

REVIEW

Open Access



Quantitative susceptibility mapping (QSM) of the cardiovascular system: challenges and perspectives

Alberto Aimo^{1,2}, Li Huang³, Andrew Tyler³, Andrea Barison^{1,2}, Nicola Martini², Luigi F. Saccaro¹, Sébastien Roujol^{3,4*}  and Pier-Giorgio Masci³

Abstract

Quantitative susceptibility mapping (QSM) is a powerful, non-invasive, magnetic resonance imaging (MRI) technique that relies on measurement of magnetic susceptibility. So far, QSM has been employed mostly to study neurological disorders characterized by iron accumulation, such as Parkinson's and Alzheimer's diseases. Nonetheless, QSM allows mapping key indicators of cardiac disease such as blood oxygenation and myocardial iron content. For this reason, the application of QSM offers an unprecedented opportunity to gain a better understanding of the pathophysiological changes associated with cardiovascular disease and to monitor their evolution and response to treatment. Recent studies on cardiovascular QSM have shown the feasibility of a non-invasive assessment of blood oxygenation, myocardial iron content and myocardial fibre orientation, as well as carotid plaque composition. Significant technical challenges remain, the most evident of which are related to cardiac and respiratory motion, blood flow, chemical shift effects and susceptibility artefacts. Significant work is ongoing to overcome these challenges and integrate the QSM technique into clinical practice in the cardiovascular field.

Keywords: QSM, Cardiac magnetic resonance, Magnetic susceptibility, Heart, Cardiovascular disease, Iron

Spatial variations in magnetic susceptibility distort magnetic fields. These magnetic field distortions commonly lead to undesirable artefacts in magnetic resonance imaging (MRI) images, but since magnetic susceptibility is related to the underlying composition of tissue it can also provide a wealth of information. One clinically efficient approach to quantifying magnetic susceptibility is to first calculate maps of the main (B_0) magnetic field, which has been distorted by the varying magnetic susceptibility of the tissue. The magnetic susceptibility distribution is then calculated from the field map, by

solving a 'field-to-source' problem. Calculation of quantitative susceptibility maps (QSM) cannot be achieved with magnitude gradient-echo images alone, instead phase images acquired at different echo times are needed to measure the B_0 maps, by first calculating the rate of phase accrual at each voxel (which is equivalent to the local frequency), then converting this to local B_0 using the Larmor equation. Although this method is technically challenging, owing to the difficulty of obtaining high fidelity B_0 maps and successfully performing the field-to-source reconstruction, QSM can provide key information on the biochemical constituents and microstructure of tissue. So far, QSM research has primarily focused on applications in neurology, particularly the identification of iron containing substances such as hemosiderin associated with hemorrhage, iron more generally, and paramagnetic contrast agents [1–7]. However, more recently,

*Correspondence: sebastien.roujol@kcl.ac.uk

⁴ Department of Biomedical Engineering, School of Imaging Sciences & Biomedical Engineering, King's College London, St Thomas' Hospital, 4th Floor Lambeth Wing, London SE1 7EH, UK
Full list of author information is available at the end of the article



major advances have also been achieved in QSM outside the central nervous system, including the abdomen [8–10], neck [11] and cardiovascular system. This review provides a critical overview of cardiovascular QSM, as a complementary technique to state-of-the-art multi-parametric cardiovascular magnetic resonance (CMR), exploring how it can improve disease phenotyping and pathophysiological understanding (Fig. 1).

Basic principles

Magnetic susceptibility measures the degree to which a material is magnetized when exposed to a homogeneous external magnetic field (H), and is expressed as a dimensionless ratio (χ) between material magnetization (M) and the external magnetic field strength (H), i.e., $\chi = M/H$ [12]. Magnetic materials are classified as either diamagnetic ($\chi < 0$), paramagnetic ($0 < \chi < 0.01$), or ferromagnetic ($\chi > 0.01$) [13]. Magnetic susceptibilities are often expressed in parts-per-million (ppm), relative to the magnetic susceptibility of water (which has an absolute magnetic susceptibility of 9×10^{-6}), this convention will be used for the remainder of the article. Biological tissues can be diamagnetic (e.g., calcium phosphate), paramagnetic (e.g., deoxyhemoglobin, copper or manganese) or ferromagnetic (iron). In CMR, the χ of an organ within the static magnetic field B_0 can be quantified by mapping the magnetic field perturbation (δB). To map χ , we first construct the forward problem that expresses how the inhomogeneous susceptibility (χ) distorts the magnetic field B_0 , after which

the inverse problem is solved. The magnetic field distortion $\delta B(\mathbf{r})$ induced by a susceptibility distribution $\chi(\mathbf{r})$ can be computed by convolving the susceptibility distribution by the unit magnetic dipole kernel $d(\mathbf{r})$, resulting in the following equation [14]

$$\delta B(\mathbf{r}) = B_0 \cdot d(\mathbf{r}) \otimes \chi(\mathbf{r}), \tag{1}$$

where B_0 is assumed to be along z -direction, \otimes is the convolution operator, and $d(\mathbf{r})$ is defined as

$$d(\mathbf{r}) = \frac{1}{4\pi} \cdot \frac{3\cos^2\theta - 1}{|\mathbf{r}|^3} \tag{2}$$

with $|\mathbf{r}|$ and θ being the radial distance and polar angle in the spherical polar coordinate system, respectively. The induced magnetic field perturbation δB map can be calculated from a Larmor resonance frequency shift ($\delta\omega$) map (measured using 3D multi-echo GRE phase images) with the following relation

$$\delta B(\mathbf{r}) = \delta\omega(\mathbf{r})/\gamma, \tag{3}$$

where γ is the gyromagnetic ratio.

Due to the spatial extent of $d(\mathbf{r})$, the measured δB depends on the magnetic susceptibility both within, and outside of the object, making it very challenging to solve Eq. 1. δB is therefore separated into two components, referring to the B_0 perturbations caused by magnetic susceptibilities located within (δB_{loc}), and outside (δB_{bkg}) of the object with

$$\delta B = \delta B_{loc} + \delta B_{bkg}. \tag{4}$$

Since δB_{loc} results from the magnetic susceptibility contribution inside the region of interest (ROI), the tissue magnetic susceptibility (χ_{tis}) inside the ROI can be calculated with the equation

$$\delta B_{loc}(\mathbf{r}) = B_0 \cdot d(\mathbf{r}) \otimes \chi_{tis}(\mathbf{r}), \tag{5}$$

which can be expressed under the k space formalism as [15].

$$\delta B_{loc}(\mathbf{k}) = B_0 \cdot d(\mathbf{k}) \cdot \chi_{tis}(\mathbf{k}), \tag{6}$$

by using the Fourier convolution theorem ($FT(a \otimes b) = FT(a) \cdot FT(b)$) [16], where

$$d(\mathbf{k}) = \frac{1}{3} - \left(\frac{k_z}{k}\right)^2 \tag{7}$$

is the dipole kernel. The 3D χ_{tis} map is reconstructed by solving this ‘field-to-source’ inverse problem. Unfortunately however, the presence of two conical surfaces at polar angles of $\pm 54.7^\circ$ to the z -axis where $d(\mathbf{k}) = 0$, prevents direct deconvolution of Eq. 6 to find χ_{tis} and

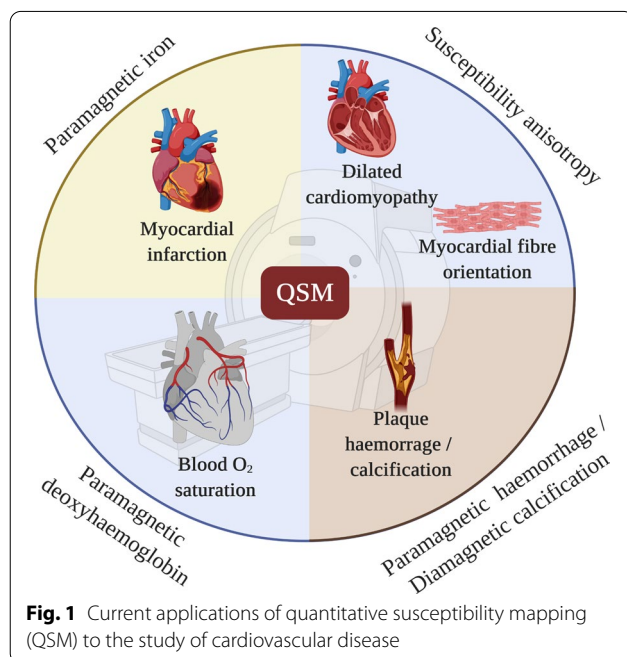


Fig. 1 Current applications of quantitative susceptibility mapping (QSM) to the study of cardiovascular disease

necessitates the use of either the Calculation Of Susceptibility through a Multiple-Orientation Sampling (COSMOS) method [17] (which is impractical due to the requirement to acquire data with the patient in multiple positions) or regularization [18–26] when solving Eq. 6.

In practice, for cardiac QSM, there are three steps to finding this 3D χ_{tis} map which are shown in Fig. 2.

- (1) Step 1: Estimation of the magnetic field perturbation map. A 3D $\delta\omega$ map is the first estimated from the phase evolution in 3D multi-echo gradient echo (GRE) CMR images; this 3D $\delta\omega$ map is then used to generate a 3D δB map according to Eq. 3. Phase unwrapping is then performed, to remove phase discontinuities, using a variety of methods including, region growing [27, 28], Laplacian [29, 30], and Best-path [31, 32] methods.
- (2) Step 2: Estimation of the local magnetic field perturbation map. A 3D δB_{loc} map is computed by removal of δB_{bkg} from the δB map based on Eq. 4, using methods such as Sophisticated Harmonic Artifact Reduction for Phase (SHARP) [33, 34], Projection onto Dipole Fields (PDF) [35], or the Laplacian Boundary Value (LBV) method [36].
- (3) Step 3: Estimation of the tissue magnetic susceptibility map. A 3D χ_{tis} map is reconstructed from

the 3D δB_{loc} map by solving the field-to-source inverse problem based on Eq. 6. Using ℓ_1 - and ℓ_2 -regularization techniques such as Morphology Enabled Dipole Inversion (MEDI) [25] or Homogeneity-Enabled Incremental Dipole Inversion (HEIDI) [26].

Biochemical foundations of QSM

QSM measures the spatial distribution of χ produced by the diamagnetic, paramagnetic and ferromagnetic constituents of tissue [6]. The body contains trace amounts of several paramagnetic transition metal ions such as copper, manganese, and cobalt. Iron is ~30 times more abundant in the body than all the other paramagnetic ions together, with an iron content of ~53 mg/kg in healthy subjects. As such, a 70 kg human contains ~3700 mg of iron, of which nearly 2500 mg are linked to haemoglobin in blood or myoglobin in skeletal muscles (heme iron), with the remainder linked to ferritin or hemosiderin (non-heme iron) [37, 38]. The magnetic susceptibility perturbations seen in human tissue depend almost entirely on non-heme iron concentration [38]. However, in healthy subjects, non-heme iron deposits are evenly distributed throughout the body and therefore result in negligible susceptibility variations. Only when

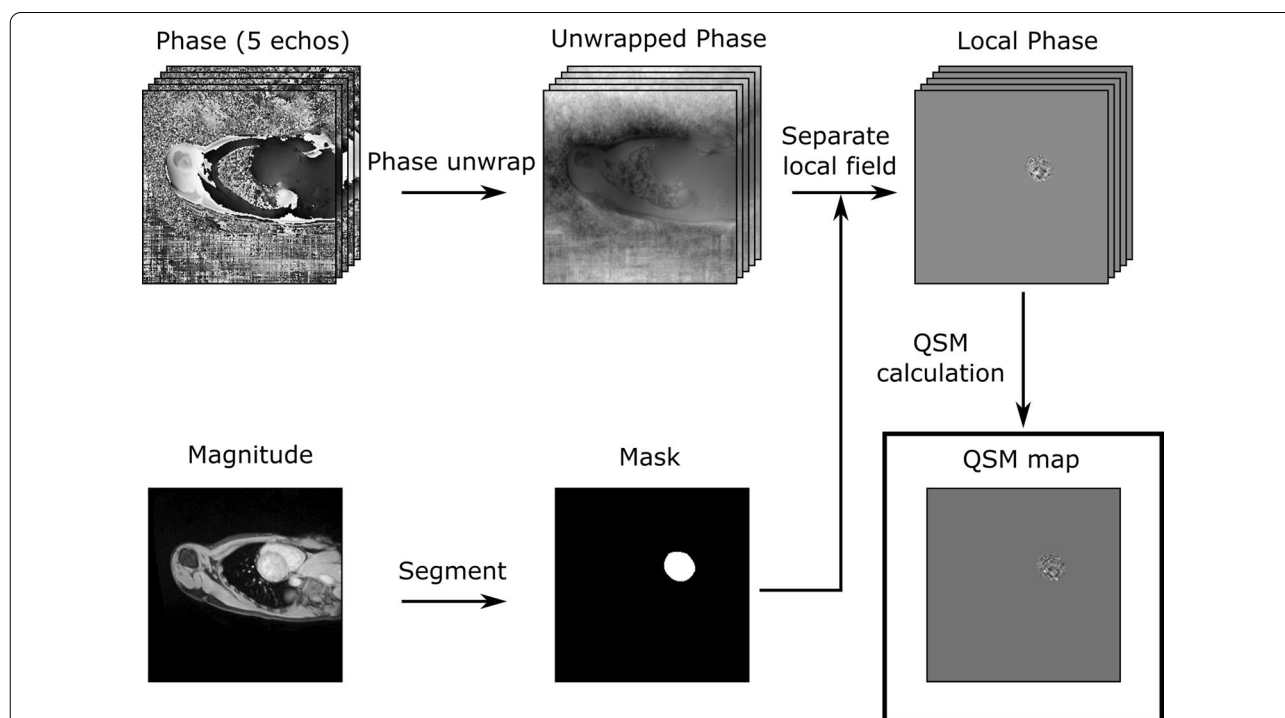


Fig. 2 Steps of quantitative susceptibility mapping (QSM) post-processing. Example left ventricular QSM maps were computed from magnitude and phase multi-echo gradient echo images. Step 1: Phase images are phase unwrapped. Step 2: The local and background fields are separated, using segmentation masks generated from the magnitude images. Step 3: The QSM map is computed from the local magnetic field map

local iron deposits equal or exceed ~ 1 mM in concentration, will a significant χ difference, compared to iron-free regions be observed with QSM, for instance of ~ 1 ppm in severe transmural myocardial infarction [39].

Although T_2^* magnitude imaging by multi-echo GRE is already a well-validated technique to quantify iron deposits, T_2^* relaxation time (or $R_2^* = 1/T_2^*$) is influenced by local background susceptibility and other sources alongside iron deposits [40]. For instance, in brain imaging T_2^* (or R_2^*) relaxivity, measured by GRE images, can miss pathological iron accumulation due to the competing effect of the diamagnetic myelin, the main white matter component [41]. The magnetic susceptibility of tissue depends upon its constituents, with each constituent's contribution depending on its electronic structure and concentration. On a molecular level, magnetic susceptibility is determined by the electronic configuration, with unpaired electrons contributing to paramagnetism. However in bio-molecules, this relationship may be less intuitive, for instance, oxyhaemoglobin, which is made up of four globular proteins each containing the Fe^{3+} -haeme, is diamagnetic despite Fe^{3+} , in aqueous solution, possessing five unpaired electrons, whereas deoxyhaemoglobin is paramagnetic [42].

Cardiovascular applications of QSM

The application of QSM for studying the cardiovascular system offers an unprecedented opportunity to gain a better understanding of the pathophysiological changes associated with cardiovascular disease. A number of state-of-the-art applications are described in the following sections, each of which has the potential to significantly improve patient care and outcomes in impactful areas of cardiac medicine. Despite this, the field of cardiac QSM is in its infancy, so a number of challenges remain to be solved. The most evident of these challenges are related to cardiac and respiratory motion, blood flow, chemical shift effects at the boundary between the epicardium and epicardial fat, and susceptibility artefacts at the myocardium-lung interface [39, 43].

Blood oxygenation

Oxygen saturation in the arterial blood (SaO_2) is a relevant biomarker in many cardiovascular diseases, and is commonly used for the identification and quantification intra-cardiac shunts in congenital heart disease. This metric also provides an index of systemic oxygen delivery and consumption in heart failure [44–46] and pulmonary hypertension [47, 48]. Recently, Wen et al. demonstrated the possibility to gauge venous SaO_2 by measuring the difference in magnetic susceptibility between the venous and arterial blood pools using QSM [43]. For this purpose, the authors used a multiple breath-hold

electrocardiogram (ECG)-gated 2D multi-echo GRE to obtain T_2^* source images that were then post-processed to generate QSM maps. The latter showed strong differential susceptibility ($\Delta\chi$) between RV and LV blood pools as a result of the paramagnetic and diamagnetic properties of the deoxygenated and oxygenated hemoglobin, respectively, which allowed them to measure of the blood oxygenation difference (ΔSaO_2) using an established formula [43]:

$$\Delta SaO_2 = \frac{\Delta\chi}{4H\chi_{deoxyheme}}$$

where $4\chi_{deoxyheme}$ is the molar susceptibility of a fully deoxygenated deoxyhemoglobin (151.054 ppb ml/ μ) and H is the heme concentration in blood, which is derived from the patient's measured hematocrit (Hct), the mass concentration of hemoglobin in a red cell ($\rho_{RBC:Hb} = 0.34$ g/ml), and the molar mass of deoxyhemoglobin ($M_{Hb} = 6444 \cdot 10^{-6}$ g/ μ mol) [49].

This approach, however, was complicated by long acquisition time, low signal-to-noise ratio (SNR) and inconsistent positioning of consecutive short-axis slices across the ventricles which lead to non-interpretatable source GRE images in 36% of subjects [43]. These limitations were resolved by adopting a free-breathing ECG-triggered navigator-gated 3D multi-echo GRE sequence which allowed the authors to generate interpretable QSM maps in all healthy subjects and 87% of patients with a reduction of acquisition time by about 30% as compared to the 2D approach (Fig. 3). In a clinical cohort ($n = 34$), patients with left ventricular (LV) dysfunction (LV ejection fraction $< 50\%$) had greater ΔSaO_2 than those with preserved systolic function. Remarkably, the 3D approach also showed an excellent correlation and small bias when compared to invasively measured ΔSaO_2 (gold-standard) in 15 patients undergoing cardiac catheterization [50]. QSM-oximetry may offer advantages to conventional methods, which rely on the T_2 , T_2^* , and T_1 relaxation times of the blood pool. For instance, the dependence of T_2 relaxation time on blood oxygenation is well established, but requires measuring multiple complex Luz–Meiboom model parameters, restricting its clinical applicability [51]. Recently, Varghese et al. introduced a promising technique that used multiple T_2 measurements, with different inter-echo pulse spacing, to estimate all the parameters in the Luz–Meiboom model and non-invasively estimate the SaO_2 [51, 52]. However, this method has shown flow dependency, with signal loss in the specific regions of the cardiac chambers, which combined with the 2D single-slice approach, leads to a dependency on user input during the acquisition and post-processing stages, with ensuing high intra- and inter-observer variability.

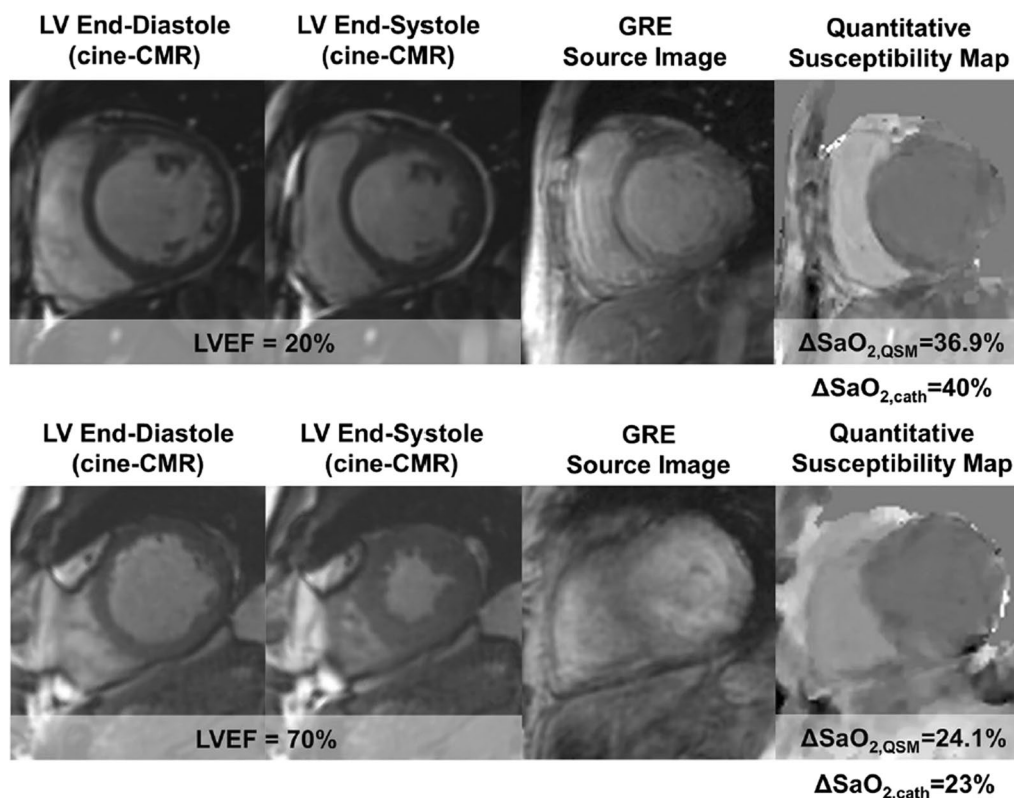


Fig. 3 Free breathing three-dimensional cardiac quantitative susceptibility mapping (QSM) in cardiac patients. Representative examples of QSM maps in two cardiac patients which are used to quantify ventricular blood oxygenation. Top: QSM map of patient heart with reduced left ventricular ejection fraction (LVEF) shows a marked difference in blood oxygen between left and right ventricles. Bottom: QSM map of patient heart with normal LVEF shows a difference in blood oxygenation between the ventricles within the normal range (Reprinted with permission from Wen et al. [50])

QSM-oxymetry has the potential to play a key role in congenital heart disease, where CMR is increasingly used for pre- and post-operative management, as an alternative to invasive catheterization. The non-invasive, ionizing-radiation free, nature of QSM-oximetry is well suited for repeated CMR exams of young patients, complementing phase-contrast velocity-encoding techniques for intra-cardiac shunt diagnosis, management, and follow-up. In addition, QSM-oximetry may provide key information in patients with heart failure or pulmonary hypertension, as well as in establishing the cause of hypoxemia, and may potentially be used to tailor therapy and monitor treatment. Mixed venous oxygen saturation ($vSaO_2$) reflects the balance between oxygen delivery and consumption; in patients with heart failure a low $vSaO_2$ is associated with advanced and decompensated hemodynamic status due to insufficient cardiac output, and/or reduced arterial oxygen saturation ($aSaO_2$). It is important to acknowledge that a substantial number of heart failure patients can have a reduced $vSaO_2$ despite a normal cardiac output [53]. Importantly, unlike cardiac

output, $sSaO_2$ has been shown to predict clinical outcomes in patients with acute myocardial infarction and patients with primary pulmonary hypertension [54, 55].

Myocardial iron

In patients with ST-segment elevation myocardial infarction (STEMI), re-opening of the infarct-related artery is a prerequisite to salvaging the ischemic myocardium. However, reperfusion per se brings about myocardial damage (ischaemia/reperfusion injury) partially negating the benefits of infarct-related artery re-opening. Intramyocardial haemorrhage (IMH) is a hallmark of severe ischemia–reperfusion injury, occurring in about half of patients with a STEMI. This phenomenon is due to the loss of coronary microvasculature integrity with ensuing erythrocyte extravasation and iron accumulation in the myocardium from hemoglobin breakdown. Compelling evidence indicates that IMH is a strong independent predictor of adverse LV remodelling and untoward clinical outcomes in STEMI patients, potentially due to the increased production of reactive oxygen

species promoted by elevated iron levels [56, 57]. This makes IMH, which can be measured indirectly via iron concentration with QSM, an ideal biomarker for testing novel cardioprotective strategies to mitigate ischemia–reperfusion injury. In a swine model of haemorrhagic infarction, QSM showed a paramagnetic shift in the infarct, reflecting an elevated tissue iron content, which was independently validated by histology, plasma optical emission spectrometry, electron paramagnetic resonance spectroscopy, and RNA analysis of markers for iron metabolism. When compared with standard iron-sensitive sequences, including T_2^* -weighted, T_2^* - or R_2^* maps, QSM showed higher diagnostic accuracy for pathological iron overload. For instance, in animals with permanent coronary occlusion QSM showed a paramagnetic shift in the infarct region, compared to a remote myocardium region, where abnormal iron concentration was confirmed by histology, spectrometry, and spectroscopy in the infarct region. This information was missed by standard T_2^* -weighted and T_2^* - or R_2^* ($1/T_2^*$) maps, which are currently used to detect and quantify IMH. This finding is not unexpected since multiple biochemical factors can exert opposite effects on T_2^* relaxation time in the acutely infarcted myocardium, including shortening due to iron, and lengthening due to edema, fat and collagen deposition. QSM however, directly probes the local magnetic susceptibility [58], which closely relates to iron concentration. This experimental proof-of-concept was replicated in a small cohort of STEMI patients, who underwent a comprehensive CMR 3 days (on average) after the re-opening of the infarct-related artery. In this cohort, the magnetic susceptibility of the infarct was significantly higher than the susceptibility of the remote myocardium for all patients [39], an important finding given the clinical relevance of IMH.

QSM may also be applicable to the assessment of patients with hemochromatosis in order to quantify myocardial iron deposition, which strongly affects LV remodelling and clinical outcome [59, 60]. Both T_1 and T_2^* maps have been used for myocardial iron quantification, although T_1 -mapping is likely better placed to capture the very early stage of cardiac hemosiderosis [61]. QSM holds the potential of representing an alternative for iron quantification in the heart, but will require validation before it can be used in the clinic, particularly given the dual-challenges of cardiac and respiratory motion. Nonetheless, seminal papers have shown that QSM is accurate, and well-suited to quantifying iron concentration in the liver, with the inherent advantage of measuring the iron concentration based upon a fundamental property of the tissue, i.e., local magnetic susceptibility, rather than extrapolating this information from empirical relaxation parameters (e.g., R_2 and R_2^*), which are affected by

other factors including fibrosis and steatosis [62]. QSM reconstruction can account for the different spectral peaks of adipose tissue to ensure an accurate estimation of the B_0 field maps which are minimally influenced by liver fibrosis or inflammation. Fat fraction and chemical shift corrected magnetic susceptibility maps can be calculated with methods such as Chemical QSM, which uses the Dixon-based IDEAL method [63]. Moreover, QSM removes the blooming artefacts in regions near the air-tissue or fat-tissue interface that typically affect R_2^* maps. Collectively, QSM appears to have comparative advantages to the current R_2^* maps used for liver iron quantification [62, 64] although further validation is required. Finally, it is also important to bear in mind that R_2^* and QSM maps are not mutually exclusive techniques since either map is reconstructed from source images acquired by 3D multi-echo GRE sequence.

Myocardial fibre orientation

The restrained distribution of molecules in a specific tissue can be gauged by magnetic susceptibility anisotropy using susceptibility tensor imaging (STI), which calculates a susceptibility tensor using multiple images with different B_0 orientations. Susceptibility anisotropy originates from the ordered (restrained) spatial arrangement of molecules with diamagnetic (e.g., calcium) and paramagnetic (e.g., iron) properties within a tissue, which then generates a bulk (macroscopic) anisotropic susceptibility. This is exemplified by the ordered distribution of phospholipids in the myelin sheaths which encapsulate axons in the central nervous system, giving rise to measurable macroscopic susceptibility anisotropy [65].

Cardiac myofibrils consist of serially repeated sarcomere units, a highly organised structure of repeated of thick and thin myofilaments oriented parallel to the long axis of the myofibril. This myocardial microstructure is altered in cardiomyopathy, myocardial infarction, and congenital heart diseases, where the initial misalignment of myocardial fibres causes increased myocardial stress, which begets further fibre misalignment and promotes adverse cardiac remodelling, eventually culminating in heart failure or life-threatening ventricular arrhythmias [66–70]. Hence, mapping myofibre organization could be an important tool for assessing the functional properties of healthy and diseased hearts. Ex-vivo, STI is able to capture myofibre orientation by harnessing the magnetic anisotropy of polypeptide bonds in the myofilaments which collectively generate bulk (macroscopic) anisotropic susceptibility on a scale measurable by QSM [71]. Myofibers perpendicular to the B_0 appear diamagnetic while those parallel to B_0 are paramagnetic relative to the reference susceptibility [72]. In the healthy heart the

contribution of collagen to magnetic susceptibility anisotropy is low, however its contribution does become significant (anti-parallel and $\sim 50\%$ magnitude of myofibril) in collagenised scars such as those found with ischemic cardiomyopathy [73]. This makes STI a promising alternative technique, if the requirement for multiple B_0 orientations can be overcome, to the most commonly used technique for mapping myofibre orientation, diffusion tensor imaging (DTI) [74]. While high-resolution cardiac DTI provides exclusively structural information (myofiber orientation), STI can combine structural and biochemical information including myocardial oxygenation and collagen content (myocardial scarring). Moreover, cardiac DTI suffers from spatial resolution limits (typically $\sim 2.7 \times 2.7 \times 6$ mm [74]), long scan times (e.g. 18 heartbeats per slice measurement in Nielles-Vallespin et al. [75]) and a low signal-to-noise ratio requiring multiple averages [75, 76]. On the other hand, STI is relatively novel, and less well validated compared to DTI, and STI reconstruction can suffer from low-frequency artefacts in the reconstructed tensor images. Several methods have been proposed to implement STI, including the incorporation of magnitude-derived relaxation and phase-derived susceptibility tensors [71], and the use of a gadolinium-based contrast agent. Gadolinium-based contrast-agent distributes in the extracellular space in normal myocardium causing rapid relaxation of water in this compartment without any change in the magnetic properties of the intracellular water. Thus, the use of gadolinium-based contrast-agent has the potential to

minimise the signal from the extracellular space leaving the anisotropic intracellular compartment to dominate tissue susceptibility [77].

QSM for atherosclerotic plaque assessment

Vulnerable atherosclerotic plaques are characterized by the presence of a lipid-rich necrotic core, intraplaque hemorrhage, a thin ruptured fibrous cap, and to a lesser degree calcification [78]. Currently, multi-contrast CMR is customary for carotid plaque characterization, with a focus on intra-plaque hemorrhage which is associated with rapid plaque progression and recurrent cerebrovascular events in patients with high-grade stenosis [79, 80]. Fresh intraplaque hemorrhage can be identified as a vessel wall region with hyperintense signal on T_1 -weighted images, while chronic intraplaque hemorrhage appears markedly hypointense on T_1 -weighted, T_2 - or T_2^* weighted, and time-of-flight images. The differentiation of chronic intraplaque hemorrhage and plaque calcification is challenging, given that both are associated with signal loss on multi-contrast CMR. In contrast, QSM can distinguish diamagnetic calcification from paramagnetic intraplaque hemorrhage [78, 81, 82], and strongly correlates with histology in patients undergoing carotid endarterectomy [83]. In this patient group calcified plaques had strongly negative susceptibility (≤ -1 ppm), whereas intraplaque hemorrhage had positive susceptibility, ranging from ~ 0.5 ppm, in a recent haemorrhage, to 1.5–2 ppm in a chronic haemorrhage (Fig. 4).

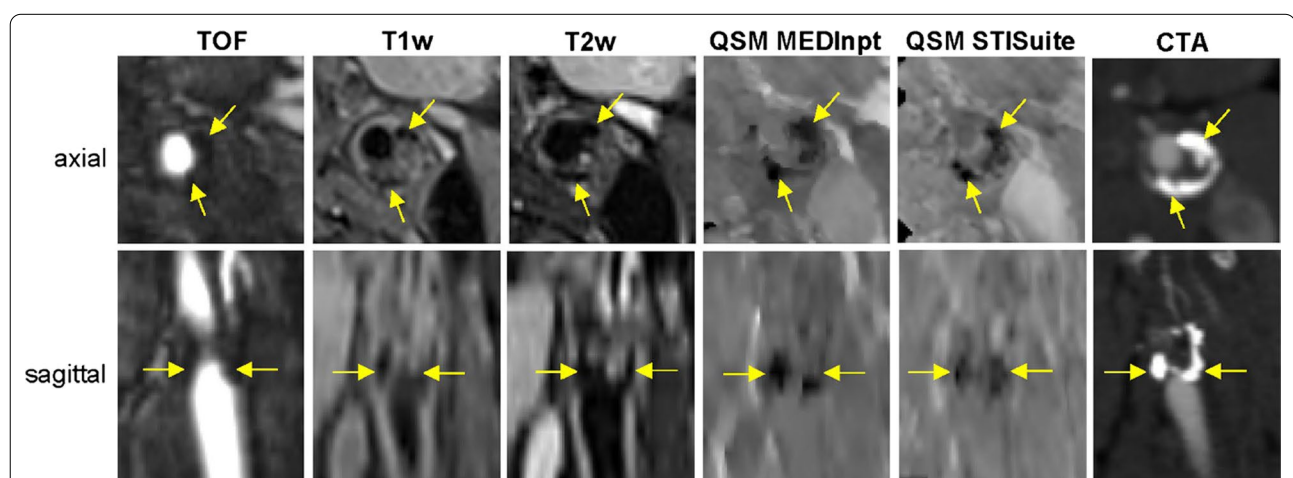


Fig. 4 Quantitative susceptibility mapping (QSM) of a carotid plaque. Example of magnetic resonance imaging of a heavily calcified plaque almost fully occluding the left internal carotid artery at the level of carotid bifurcation with hypointense appearance on time-of-flight (TOF) and black-blood T_1 -weighted (T_1w) and T_2 -weighted (T_2w) images as well as strongly negative susceptibility on QSM images computed with MEDInpt and the STISuite. The computed tomography angiography (CTA) image acquired 1.5 years before CMR at 0.6-mm resolution from the same patient is shown to help with plaque localization (Reprinted with permission from: Nguyen et al. [82])

Ultra-small superparamagnetic iron oxide (USPIO) contrast agents are increasingly used to measure macrophage infiltration. After intravenous injection, this compound enters plaque through its leaky endothelium and is internalised by macrophages. Comparison of pre- and post-USPIO iron-sensitive sequences, such as T_2^* -weighted or R_2^* -maps, enables the quantification of the inflammatory component of atherosclerotic plaque. Recent studies indicate that QSM implemented with IDEAL water-fat separation can concurrently identify multiple high-risk plaque features (calcification, intra-plaque haemorrhage, lipid-rich necrotic core and USPIO uptake), moreover, the addition of IDEAL improves QSM image quality reducing the streaking artefacts caused by chemical frequency shift. Thus, QSM processing could fit within a multi-contrast approach for quantification of atherosclerosis using a single 3D multi-echo GRE acquisition [84], eliminating the need for a time-consuming, and error-prone, multi-contrast CMR exam.

Future challenges in cardiovascular QSM

Despite the recent breakthroughs in QSM, accurate quantification of magnetic susceptibility is still challenging. Existing methods need to be evaluated systematically under a variety of experimental conditions, and further work is needed to achieve high degrees of consistency. Blood flow and motion cause phase variations that can lead to erroneous magnetic field estimates. Chemical shift, proton exchange and partial volume effect can also influence frequency shift, introducing further errors. Currently, 3D multi-echo GRE acquisition, with a diaphragmatic navigator, is preferred to the breath-hold multi-slice 2D approach as this prevents slice misalignment and non-continuous k-space sampling. However, standard diaphragmatic navigators rely on a tracking factor (commonly set to 0.6) to correct for diaphragmatic and heart motions. Typical navigator gating efficiency (~25–60%) and the tracking factor is known to be subject-dependent and highly variable. Prospective respiratory gating techniques may provide higher gating efficiency (up to 100%) and improve motion correction using complex subject-specific models of the diaphragmatic/heart motion relationship [85–87] or image-based navigators which directly track heart motion [88, 89]. However, the respiration induces local magnetic susceptibility variations which may introduce errors in the QSM reconstruction if data are prospectively acquired at different respiratory phases.

Epicardial fat represents another challenge in cardiovascular QSM. However, Dixon-based fat-water separation methods, such as IDEAL, have been successfully adopted in abdomen or neck QSM [62, 84] and may offer advantages for cardiac QSM as well. However, these

techniques rely upon prior knowledge of chemical spectrum which may be influenced by a variety of factors such as lipid compartmentalization and fatty acids content. Recent techniques have been proposed to supersede this limitation, by correcting QSM for chemical shift map during reconstruction [63]. Another challenge to cardiovascular QSM is the high susceptibility at the interface of cardiac structures and lungs. However, several methods have been successfully applied for background phase removal in neck and abdominal QSM [62, 84] which could be integrated in the cardiovascular QSM pipeline, compensating for deficient B_0 shimming [43]. Nonetheless, the numerical inconsistency of QSM in varying B_0 shimming conditions still exists due to short T_2^* decay, and this issue is particularly relevant in higher magnetic fields (3T/7T), requiring higher-order shimming. Most current cardiovascular QSM literature is based on single-centre studies and there is currently insufficient data characterizing the technique's accuracy, repeatability, and reproducibility (both within a given site/scanner and between sites/scanners). Different experimental setups may influence QSM, including the choice of the QSM reconstruction algorithm, imaging parameter selection, field strength, and shimming approaches/shim set performance. Therefore, the development of a commercially available QSM phantom together with the site-specific estimation of reference QSM values in healthy subjects/patients may be necessary for calibration and standardization purposes, as is currently the case in other areas such as myocardial T_1 mapping [90]. Current reconstruction algorithms are often performed offline and retrospectively, due to computational cost. The design of fast reconstruction algorithms or the use of advanced computing hardware such as graphical processing units, increasingly available on commercial scanners, may represent a promising direction to reduce computational cost. Finally, machine learning techniques, based on convolutional neural networks are under active development for each stage of the QSM pipeline [91]. Examples include, PhaseNet 2.0 [92] for phase unwrapping, SHARQnet [93], for the separation of local and background fields, and QSMnet⁺ [94] for calculating magnetic susceptibility. These techniques may offer advantages over traditional algorithmic reconstruction techniques beyond reconstruction acceleration, including improved accuracy, robustness, and automation (e.g. automatic image segmentation), all of which have the potential to improve clinical utility and uptake.

Conclusions

QSM is a promising method to expand the arsenal of measurable, reproducible and accurate CMR biomarkers in the heart, and therefore enable better understanding of

the intricate pathophysiology processes underlying cardiovascular diseases. However, overcoming outstanding technical challenges and validation in large clinical studies are critical steps for a successful integration of cardiovascular QSM into clinical practice.

Abbreviations

B_0 : Main magnetic field; CMR: Cardiovascular magnetic resonance; COSMOS: Calculation Of Susceptibility through a Multiple-Orientation Sampling; DTI: Diffusion tensor imaging; ECG: Electrocardiogram; GRE: Gradient echo; HEIDI: Homogeneity-Enabled Incremental Dipole Inversion; IMH: Intramyocardial haemorrhage; LBV: Laplacian Boundary Value; LV: Left ventricle/left ventricular; LVEF: Left ventricular ejection fraction; MEDI: Morphology Enabled Dipole Inversion; MRI: Magnetic resonance imaging; QSM: Quantitative susceptibility mapping; PDF: Projection onto Dipole Fields; ROI: Region of interest; SO_2 : Oxygen saturation in the arterial blood; SHARP: Sophisticated Harmonic Artifact Reduction for Phase; STEMI: ST-segment elevation myocardial infarction; STI: Susceptibility tensor imaging; USPIO: Ultra-small superparamagnetic iron oxide; vSO_2 : Mixed venous oxygen saturation.

Acknowledgements

None.

Author contributions

AA, LH, AB, NM, LFS: writing, original draft; AT, SR, P-GM: critical revision. All authors read and approved the final manuscript.

Funding

The authors (SR, LH, AT) are supported in part by the Engineering and Physical Sciences Research Council (EPSRC) Grant (EP/R010935/1) and the British Heart Foundation (BHF) Grants (PG/19/11/34243 and PG/21/10539).

Availability of data and materials

Not applicable.

Declarations

Ethics approval and consent to participate

Not applicable.

Consent for publication

Not applicable.

Competing interests

The authors declare that they have no competing interests.

Author details

¹Scuola Superiore Sant'Anna, Pisa, Italy. ²Fondazione Toscana Gabriele Monasterio, Pisa, Italy. ³School of Biomedical Engineering and Imaging Sciences, King's College London, London, UK. ⁴Department of Biomedical Engineering, School of Imaging Sciences & Biomedical Engineering, King's College London, St Thomas' Hospital, 4th Floor Lambeth Wing, London SE1 7EH, UK.

Received: 28 April 2022 Accepted: 5 August 2022

Published online: 18 August 2022

References

- Schweser F, et al. Differentiation between diamagnetic and paramagnetic cerebral lesions based on magnetic susceptibility mapping. *Med Phys*. 2010;37(10):5165–78.
- Chen W, et al. Intracranial calcifications and hemorrhages: characterization with quantitative susceptibility mapping. *Radiology*. 2014;270(2):496–505.
- Berberat J, et al. Differentiation between calcification and hemorrhage in brain tumors using susceptibility-weighted imaging: a pilot study. *Am J Roentgenol*. 2014;202(4):847–50.
- Ciraci S, et al. Diagnosis of intracranial calcification and hemorrhage in pediatric patients: comparison of quantitative susceptibility mapping and phase images of susceptibility-weighted imaging. *Diagn Interv Imaging*. 2017;98(10):707–14.
- Xu M, et al. Brain iron assessment in patients with First-episode schizophrenia using quantitative susceptibility mapping. *Neuroimage Clin*. 2021;31:102736.
- Langkammer C, et al. Quantitative susceptibility mapping (QSM) as a means to measure brain iron? A post mortem validation study. *Neuroimage*. 2012;62(3):1593–9.
- Lind E, et al. Dynamic contrast-enhanced QSM for perfusion imaging: a systematic comparison of DeltaR2* and QSM-based contrast agent concentration time curves in blood and tissue. *MAGMA*. 2020;33(5):663–76.
- Sharma SD, et al. Quantitative susceptibility mapping in the abdomen as an imaging biomarker of hepatic iron overload. *Magn Reson Med*. 2015;74(3):673–83.
- Bechler E, Stabinska J, Wittsack HJ. Analysis of different phase unwrapping methods to optimize quantitative susceptibility mapping in the abdomen. *Magn Reson Med*. 2019;82(6):2077–89.
- Bechler E, et al. Feasibility of quantitative susceptibility mapping (QSM) of the human kidney. *MAGMA*. 2021;34(3):389–97.
- Karsa A, Punwani S, Shmueli K. An optimized and highly repeatable MRI acquisition and processing pipeline for quantitative susceptibility mapping in the head-and-neck region. *Magn Reson Med*. 2020;84(6):3206–22.
- Liu C, et al. Quantitative susceptibility mapping: contrast mechanisms and clinical applications. *Tomography*. 2015;1(1):3–17.
- Schenk JF. The role of magnetic susceptibility in magnetic resonance imaging: MRI magnetic compatibility of the first and second kinds. *Med Phys*. 1995;23(6):815–50.
- Ruetten PPR, Gillard JH, Graves MJ. Introduction to quantitative susceptibility mapping and susceptibility weighted imaging. *Br J Radiol*. 2019;92(1101):20181016.
- Marques JP, Bowtell R. Application of a Fourier-based method for rapid calculation of field inhomogeneity due to spatial variation of magnetic susceptibility. *Concepts Magn Reson Part B Magn Reson Eng*. 2005;25B(1):65–78.
- Haacke EM, et al. *Magnetic resonance imaging: physical principles and sequence design*. Hoboken: Wiley-Liss; 1999.
- Liu T, et al. Calculation of susceptibility through multiple orientation sampling (COSMOS): a method for conditioning the inverse problem from measured magnetic field map to susceptibility source image in MRI. *Magn Reson Med*. 2009;61(1):196–204.
- Schweser F, et al. An illustrated comparison of processing methods for phase MRI and QSM: removal of background field contributions from sources outside the region of interest. *NMR Biomed*. 2017;30(4):e3604.
- Wang Y, Liu T. Quantitative susceptibility mapping (QSM): decoding MRI data for a tissue magnetic biomarker. *Magn Reson Med*. 2015;73(1):82–101.
- Shmueli K, et al. Magnetic susceptibility mapping of brain tissue in vivo using MRI phase data. *Magn Reson Med*. 2009;62(6):1510–22.
- Wharton S, Schäfer A, Bowtell R. Susceptibility mapping in the human brain using threshold-based k-space division. *Magn Reson Med*. 2010;63(5):1292–304.
- Kressler B, et al. Nonlinear regularization for per voxel estimation of magnetic susceptibility distributions from MRI field maps. *IEEE Trans Med Imaging*. 2010;29(2):273–81.
- Wang Y, et al. Magnetic source MRI: a new quantitative imaging of magnetic biomarkers. *Annu Int Conf IEEE Eng Med Biol Soc*. 2009;2009:53–6.
- Bilgic B, et al. Fast quantitative susceptibility mapping with L1-regularization and automatic parameter selection. *Magn Reson Med*. 2014;72(5):1444–59.
- Liu T, et al. Morphology enabled dipole inversion (MEDI) from a single-angle acquisition: comparison with COSMOS in human brain imaging. *Magn Reson Med*. 2011;66(3):777–83.
- Schweser F, et al. Quantitative susceptibility mapping for investigating subtle susceptibility variations in the human brain. *Neuroimage*. 2012;62(3):2083–100.

27. Jenkinson M. Fast, automated, N-dimensional phase-unwrapping algorithm. *Magn Reson Med*. 2003;49(1):193–7.
28. Robinson S, Schödl H, Trattng S. A method for unwrapping highly wrapped multi-echo phase images at very high field: UMPIRE. *Magn Reson Med*. 2014;72(1):80–92.
29. Li W, et al. Integrated Laplacian-based phase unwrapping and background phase removal for quantitative susceptibility mapping. *NMR Biomed*. 2014;27(2):219–27.
30. Schofield MA, Zhu Y. Fast phase unwrapping algorithm for interferometric applications. *Opt Lett*. 2003;28(14):1194–6.
31. Abdul-Rahman HS, et al. Fast and robust three-dimensional best path phase unwrapping algorithm. *Appl Opt*. 2007;46(26):6623–35.
32. Abdul-Rahman H, et al. Robust three-dimensional best-path phase-unwrapping algorithm that avoids singularity loops. *Appl Opt*. 2009;48(23):4582–96.
33. Schweser F, et al. Quantitative imaging of intrinsic magnetic tissue properties using MRI signal phase: an approach to in vivo brain iron metabolism? *Neuroimage*. 2011;54(4):2789–807.
34. Li W, Wu B, Liu C. Quantitative susceptibility mapping of human brain reflects spatial variation in tissue composition. *Neuroimage*. 2011;55(4):1645–56.
35. Liu T, et al. A novel background field removal method for MRI using projection onto dipole fields (PDF). *NMR Biomed*. 2011;24(9):1129–36.
36. Zhou D, et al. Background field removal by solving the Laplacian boundary value problem. *NMR Biomed*. 2014;27(3):312–9.
37. Abbaspour N, Hurrell R, Kelishadi R. Review on iron and its importance for human health. *J Res Med Sci*. 2014;19(2):164–74.
38. Brass SD, et al. Magnetic resonance imaging of iron deposition in neurological disorders. *Top Magn Reson Imaging*. 2006;17(1):31–40.
39. Moon BF, et al. Iron imaging in myocardial infarction reperfusion injury. *Nat Commun*. 2020;11(1):3273.
40. Hirsch NM, Preibisch C. T2* mapping with background gradient correction using different excitation pulse shapes. *Am J Neuroradiol*. 2013;34(6):E65–8.
41. Bagnato F, et al. Untangling the R2* contrast in multiple sclerosis: a combined MRI-histology study at 70 Tesla. *PLoS ONE*. 2018;13(3):e0193839.
42. Liu C, et al. Susceptibility-weighted imaging and quantitative susceptibility mapping in the brain. *J Magn Reson Imaging*. 2015;42(1):23–41.
43. Wen Y, et al. Cardiac quantitative susceptibility mapping (QSM) for heart chamber oxygenation. *Magn Reson Med*. 2018;79(3):1545–52.
44. Gallet R, et al. Prognosis value of central venous oxygen saturation in acute decompensated heart failure. *Arch Cardiovasc Dis*. 2012;105(1):5–12.
45. Swiston JR, Johnson SR, Granton JT. Factors that prognosticate mortality in idiopathic pulmonary arterial hypertension: a systematic review of the literature. *Respir Med*. 2010;104(11):1588–607.
46. Sandoval J, et al. Survival in primary pulmonary hypertension. Validation of a prognostic equation. *Circulation*. 1994;89(4):1733–44.
47. Mullens W, et al. Prognostic evaluation of ambulatory patients with advanced heart failure. *Am J Cardiol*. 2008;101(9):1297–302.
48. Patel CB, et al. Characteristics and outcomes of patients with heart failure and discordant findings by right-sided heart catheterization and cardiopulmonary exercise testing. *Am J Cardiol*. 2014;114(7):1059–64.
49. Dickerson RE, Geis I. Hemoglobin: structure, function, evolution, and pathology. San Francisco: Benjamin-Cummings Publishing Company; 1983.
50. Wen Y, et al. Free breathing three-dimensional cardiac quantitative susceptibility mapping for differential cardiac chamber blood oxygenation—initial validation in patients with cardiovascular disease inclusive of direct comparison to invasive catheterization. *J Cardiovasc Magn Reson*. 2019;21(1):70.
51. Varghese J, et al. CMR-based blood oximetry via multi-parametric estimation using multiple T2 measurements. *J Cardiovasc Magn Reson*. 2017;19(1):88.
52. Varghese J, et al. Patient-adaptive magnetic resonance oximetry: comparison with invasive catheter measurement of blood oxygen saturation in patients with cardiovascular disease. *J Magn Reson Imaging*. 2020;52(5):1449–59.
53. van Beest P, et al. Clinical review: use of venous oxygen saturations as a goal—a yet unfinished puzzle. *Crit Care*. 2011;15(5):232.
54. Raymond RJ, et al. Echocardiographic predictors of adverse outcomes in primary pulmonary hypertension. *J Am Coll Cardiol*. 2002;39(7):1214–9.
55. Sumimoto T, et al. Mixed venous oxygen saturation as a guide to tissue oxygenation and prognosis in patients with acute myocardial infarction. *Am Heart J*. 1991;122(1 Pt 1):27–33.
56. Heusch G, Gersh BJ. The pathophysiology of acute myocardial infarction and strategies of protection beyond reperfusion: a continual challenge. *Eur Heart J*. 2017;38(11):774–84.
57. Betgem RP, et al. Intramyocardial haemorrhage after acute myocardial infarction. *Nat Rev Cardiol*. 2015;12(3):156–67.
58. Lotan CS, et al. The effect of postinfarction intramyocardial hemorrhage on transverse relaxation time. *Magn Reson Med*. 1992;23(2):346–55.
59. Marsella M, et al. Cardiac iron and cardiac disease in males and females with transfusion-dependent thalassemia major: a T2* magnetic resonance imaging study. *Haematologica*. 2011;96(4):515–20.
60. Meloni A, et al. Cardiac iron overload in sickle-cell disease. *Am J Hematol*. 2014;89(7):678–83.
61. Alam MH, et al. T1 at 1.5T and 3T compared with conventional T2* at 1.5T for cardiac siderosis. *J Cardiovasc Magn Reson*. 2015;17:102.
62. Sharma SD, et al. MRI-based quantitative susceptibility mapping (QSM) and R2* mapping of liver iron overload: comparison with SQUID-based biomagnetic liver susceptometry. *Magn Reson Med*. 2017;78(1):264–70.
63. Dimov AV, et al. Joint estimation of chemical shift and quantitative susceptibility mapping (chemical QSM). *Magn Reson Med*. 2015;73(6):2100–10.
64. Jafari R, et al. Rapid automated liver quantitative susceptibility mapping. *J Magn Reson Imaging*. 2019;50(3):725–32.
65. Li W, et al. Magnetic susceptibility anisotropy of human brain in vivo and its molecular underpinnings. *Neuroimage*. 2012;59(3):2088–97.
66. Tezuka F. Muscle fiber orientation in normal and hypertrophied hearts. *Tohoku J Exp Med*. 1975;117(3):289–97.
67. Wickline SA, et al. Structural remodeling of human myocardial tissue after infarction. Quantification with ultrasonic backscatter. *Circulation*. 1992;85(1):259–68.
68. Strijkers GJ, et al. Diffusion tensor imaging of left ventricular remodeling in response to myocardial infarction in the mouse. *NMR Biomed*. 2009;22(2):182–90.
69. Fenton F, Karma A. Vortex dynamics in three-dimensional continuous myocardium with fiber rotation: filament instability and fibrillation. *Chaos*. 1998;8(1):20–47.
70. Hsu EW, et al. Magnetic resonance myocardial fiber-orientation mapping with direct histological correlation. *Am J Physiol*. 1998;274(5):H1627–34.
71. Dibb R, Liu C. Joint eigenvector estimation from mutually anisotropic tensors improves susceptibility tensor imaging of the brain, kidney, and heart. *Magn Reson Med*. 2017;77(6):2331–46.
72. Dibb R, Qi Y, Liu C. Magnetic susceptibility anisotropy of myocardium imaged by cardiovascular magnetic resonance reflects the anisotropy of myocardial filament α -helix polypeptide bonds. *J Cardiovasc Magn Reson*. 2015;17(1):60.
73. Worcester DL. Structural origins of diamagnetic anisotropy in proteins. *Proc Natl Acad Sci USA*. 1978;75(11):5475–7.
74. Khalique Z, et al. Diffusion tensor cardiovascular magnetic resonance imaging: a clinical perspective. *JACC Cardiovasc Imaging*. 2020;13(5):1235–55.
75. NIELLES-VALLESPIN S, et al. In vivo diffusion tensor MRI of the human heart: reproducibility of breath-hold and navigator-based approaches. *Magn Reson Med*. 2013;70(2):454–65.
76. Scott AD, et al. An in-vivo comparison of stimulated-echo and motion compensated spin-echo sequences for 3 T diffusion tensor cardiovascular magnetic resonance at multiple cardiac phases. *J Cardiovasc Magn Reson*. 2018;20(1):1.
77. Adzamlı İK, et al. The effect of gadolinium DTPA on tissue water compartments in slow- and fast-twitch rabbit muscles. *Magn Reson Med*. 1989;11(2):172–81.
78. Arbab-Zadeh A, Fuster V. From detecting the vulnerable plaque to managing the vulnerable patient: JACC state-of-the-art review. *J Am Coll Cardiol*. 2019;74(12):1582–93.
79. Sun J, et al. Sustained acceleration in carotid atherosclerotic plaque progression with intraplaque hemorrhage: a long-term time course study. *JACC Cardiovasc Imaging*. 2012;5(8):798–804.

80. Altaf N, et al. Carotid intraplaque hemorrhage predicts recurrent symptoms in patients with high-grade carotid stenosis. *Stroke*. 2007;38(5):1633–5.
81. Wang C, et al. Quantitative susceptibility mapping for characterization of intraplaque hemorrhage and calcification in carotid atherosclerotic disease. *J Magn Reson Imaging*. 2020;52(2):534–41.
82. Nguyen TD, et al. Quantitative susceptibility mapping of carotid plaques using nonlinear total field inversion: Initial experience in patients with significant carotid stenosis. *Magn Reson Med*. 2020;84(3):1501–9.
83. Ikebe Y, et al. Quantitative susceptibility mapping for carotid atherosclerotic plaques: a pilot study. *Magn Reson Med Sci*. 2020;19(2):135–40.
84. Ruettgen PPR, et al. Simultaneous MRI water-fat separation and quantitative susceptibility mapping of carotid artery plaque pre- and post-ultrasmall superparamagnetic iron oxide-uptake. *Magn Reson Med*. 2020;84(2):686–97.
85. Bush MA, et al. Patient specific prospective respiratory motion correction for efficient, free-breathing cardiovascular MRI. *Magn Reson Med*. 2019;81(6):3662–74.
86. Mooiweer R, et al. A fast navigator (fastNAV) for prospective respiratory motion correction in first-pass myocardial perfusion imaging. *Magn Reson Med*. 2021;85(5):2661–71.
87. Moghari MH, et al. Subject-specific estimation of respiratory navigator tracking factor for free-breathing cardiovascular MR. *Magn Reson Med*. 2012;67(6):1665–72.
88. Henningsson M, et al. Prospective respiratory motion correction for coronary MR angiography using a 2D image navigator. *Magn Reson Med*. 2013;69(2):486–94.
89. Henningsson M, et al. Whole-heart coronary MR angiography with 2D self-navigated image reconstruction. *Magn Reson Med*. 2012;67(2):437–45.
90. Captur G, et al. A medical device-grade T1 and ECV phantom for global T1 mapping quality assurance—the T(1) Mapping and ECV Standardization in cardiovascular magnetic resonance (T1MES) program. *J Cardiovasc Magn Reson*. 2016;18(1):58.
91. Jung W, Bollmann S, Lee J. Overview of quantitative susceptibility mapping using deep learning: current status, challenges and opportunities. *NMR Biomed*. 2022;35(4):e4292.
92. Spoorthi GE, Gorthi RKSS, Gorthi S. PhaseNet 2.0: phase unwrapping of noisy data based on deep learning approach. *IEEE Trans Image Process*. 2020;29:4862–72.
93. Bollmann S, et al. SHARQnet—sophisticated harmonic artifact reduction in quantitative susceptibility mapping using a deep convolutional neural network. *bioRxiv*, 2019. p. 522151.
94. Jung W, et al. Exploring linearity of deep neural network trained QSM: QSMnet+. *Neuroimage*. 2020;211:116619.

Publisher's Note

Springer Nature remains neutral with regard to jurisdictional claims in published maps and institutional affiliations.

Ready to submit your research? Choose BMC and benefit from:

- fast, convenient online submission
- thorough peer review by experienced researchers in your field
- rapid publication on acceptance
- support for research data, including large and complex data types
- gold Open Access which fosters wider collaboration and increased citations
- maximum visibility for your research: over 100M website views per year

At BMC, research is always in progress.

Learn more biomedcentral.com/submissions

